Frontiers of Information Technology & Electronic Engineering
www.jzus.zju.edu.cn; engineering.cae.cn; www.springerlink.com
ISSN 2095-9184 (print); ISSN 2095-9230 (online)
E-mail: jzus@zju.edu.cn

Damage quantitative assessment of spacecraft in a large-size inspection

Kuo ZHANG[1], Jianliang HUO[†‡2], Shengzhe WANG[2], Xiao ZHANG[2], Yiting FENG[1]

[1]*School of Automation Engineering, University of Electronic Science and Technology of China, Chengdu 611731, China*

[2]*Norla Institute of Technical Physics, Chengdu 610041, China*

[†]E-mail: huoliaang@163.com

Received Dec. 30, 2020; Revision accepted Sept. 29, 2021; Crosschecked Jan. 25, 2022

Abstract: To ensure the safety and reliability of spacecraft during multiple space missions, it is necessary to conduct in-situ nondestructive detection of the spacecraft to judge the damage caused by the hypervelocity impact of micrometeoroids and orbital debris (MMOD). In this paper, we propose an innovative quantitative assessment method based on damage reconstructed image mosaic technology. First, a Gaussian mixture model clustering algorithm is applied to extract images that highlight damage characteristics. Then, a mosaicking scheme based on the ORB feature extraction algorithm and an improved M-estimator SAmple Consensus (MSAC) algorithm with an adaptive threshold selection method is proposed which can create large-scale mosaicked images for damage detection. Eventually, to create the mosaicked images, the damage characteristic regions are segmented and extracted. The location of the damage area is determined and the degree of damage is judged by calculating the centroid position and the perimeter quantitative parameters. The efficiency and applicability of the proposed method are verified by the experimental results.

Key words: Hypervelocity impact; Damage information extraction; Image mosaicking; Damage localization; Quantitative assessment

https://doi.org/10.1631/FITEE.2000733 **CLC number:** TP391

1 Introduction

With increasing human activities in space, more and more satellites, rockets, and probes are launched into the Earth orbit. Consequently, the risk of hypervelocity impact (HVI) caused by meteoroid/orbital debris (M/OD) continues to rise and it has become a major threat to space activities of spacecraft. This will also have a great impact on spacecraft, including the damage caused by surface craters and embedded impurities (Lamb, 2018; Adushkin et al., 2020; Huang et al., 2020). Considering the uncertainty of the occurrence of a spacecraft HVI event, the impact damage has high complexity. Therefore, it is necessary to adopt effective nondestructive testing techniques and to evaluate the potential damage to the spacecraft.

The optical pulsed thermography (OPT) method has been widely used due to its high efficiency, high safety, and low loss (Cheng et al., 2018; Kaur and Mulaveesala, 2020; Dua et al., 2021). In the OPT detection system, Smurov et al. (2016) and Karnati and Liou (2020) used infrared camera (IR camera) to record the distributions of Joule heat which present different transient thermal responses (TTRs) in the detection area as infrared thermal data. Recently, algorithms for extracting characteristic information from thermal data have been studied, such as independent component analysis (ICA) and principal component analysis (PCA) (Rajic, 2002; Khan et al., 2008; Gao et al., 2014; Liang

‡ Corresponding author
ORCID: Kuo ZHANG, https://orcid.org/0000-0003-1901-9951; Jianliang HUO, https://orcid.org/0000-0002-0526-8087

et al., 2016). Huang et al. (2018) introduced a rapid adaptive method of removing redundant data. Yin et al. (2021) proposed an improved method of automatically identifying the defect. Zhang HN et al. (2020) discussed the use of the variable interval to search for thermal feature components.

Many scholars have proposed quantitative methods for assessing damage information in different platforms and solution contexts. Li et al. (2019) characterized the impact damage types using passive thermography and facilitated the identification of impact damage mode and the evaluation of damage degree based on hot spot characteristics. Yin et al. (2019) proposed a novel HVI damage evaluation method based on an active infrared thermal wave image detection technology with multi-objective feature extraction optimization to achieve quantitative evaluation of M/OD HVI damages.

However, none of the above methods can meet the requirements of large-scale detection, and they have strict requirements for detection conditions. Because spacecraft are so large, it is impossible to completely understand all the damage information (such as distribution and extent) due to the limited range of a single shot. To extract damage information and reconstruct it in two-dimensional images which are easier to process, we refer to large-scale remote sensing image processing methods (Surya Kumari and Bhavani, 2017; Laraqui et al., 2018; Zhang WP et al., 2018), and apply a mosaicking method to detect a wide area of spacecraft surface.

The method based on feature points is widely used and has better performance because of its high detection speed and low computational complexity. Among the diverse feature-based methods, scale invariant feature transform (SIFT) and speeded-up robust feature (SURF) are two of the most popular feature extraction algorithms. These algorithms can maintain the scaling and rotation invariance of images and are robust to noise, displacements, geometric deformation, and illumination (Lowe, 2004; Bay et al., 2008). In conventional mosaicking schemes, for feature matching the distance ratio method and the RANdom SAmple Consensus (RANSAC) or M-estimator SAmple Consensus (MSAC) algorithm are often adopted to find the matched point pairs after screening and to estimate the geometric transformation matrix model parameters to realize the image mosaicking process (Richter et al., 2014; Magri and Fusiello, 2017). Traditional schemes rely on the experience of researchers to select the iterative threshold for screening the correct matching point combination, which is inaccurate and not universal. It is of great significance to use the optimization algorithm to calculate the appropriate threshold value to ensure matching point accuracy and save manpower.

Color features directly reflect different damage characteristics, so we can preliminarily extract damage regions by the color image segmentation method. The limitation of the classic RGB color space is that the three colors have significant linear correlation. In contrast, the $L^*a^*b^*$ (Lab for simplification) color space is the most uniform color space independent of equipment because of its uniformity on the perception level. Therefore, the Euclidean distance can be used as the metric criterion in the Lab color space, to further realize color feature segmentation using a classification algorithm (Chandrakanth and Sandhya, 2015; Fida et al., 2017).

Based on the clustering idea, in this study a Gaussian mixture model (GMM) is introduced to classify and divide data information according to the TTRs, and to separate images that highlight damage information (Chen et al., 2015; Qiu et al., 2019). The damage characteristics are extracted from the infrared thermal video to reconstruct the damage image. Then the ORB algorithm, which has high feature point detection efficiency, is adopted, and an optimized MSAC feature-matching algorithm based on an adaptive threshold selection method is proposed to obtain an accurate set of matching points to ensure the correctness of the mosaicking results (Rublee et al., 2011). Finally, the damage area is further segmented and extracted, and the location and quantitative calculations are performed on it. The efficiency and applicability of the quantitative assessment scheme are verified by the results.

2 Problem statement and presentation

In this study, we aim at achieving a rapid and effective quantitative assessment of spacecraft damage while meeting the needs of large-scale detection, and propose three main processing modules to deal with the three key issues shown in Fig. 1. They are based on damage information extraction, mosaic technology for damage image reconstruction, and quantitative assessment.

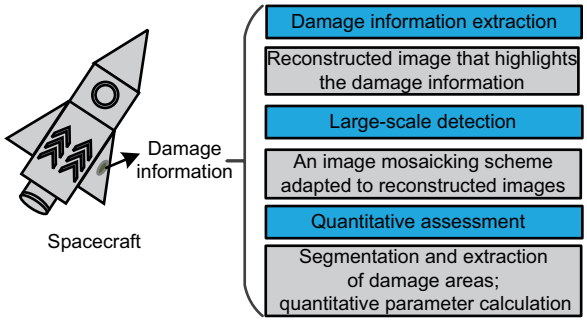

Fig. 1 Schematic of the key issues

The main innovations and contributions of this paper are as follows: (1) Based on the idea of clustering, we classify and extract damage information from the infrared thermal data, and reconstruct it in a two-dimensional image highlighting the damaged area; (2) We introduce an innovative use of mosaic technology based on damage reconstructed images, which can satisfy the large-scale detection requirement; (3) A new quantitative assessment method is effectively applied to spacecraft damage detection.

3 Damage reconstruction module

3.1 Damage information extraction

The thermal video information is sampled as the image sequence Is(f) with a certain number of frames ($f = 1, 2, ..., F_1$). The frame-by-frame change of each pixel is denoted as a TTR. Then, we vectorize each image frame and combine them into a reconstruction matrix $\boldsymbol{O}_{\rm ttr}$ with the dimension of $F_1 \times F_2$, where $F_2 = 1, 2, ..., p \times q$ and $p \times q$ is determined by the infrared camera resolution. Figs. 2a–2d show the data conversion. Each column of the reconstruction matrix $\boldsymbol{O}_{\rm ttr}$ is the corresponding TTR of a pixel, so $\boldsymbol{O}_{\rm ttr}$ can be regarded as the TTR data composed of multiple characteristic regions. Based on the TTR characteristics, the typical TTRs with the same patterns are similar and can be classified.

The thermal data can be approximated using a GMM composed of TTRs in various characteristic regions, so we can use the GMM algorithm which can describe the probability distribution of several Gaussian components to classify $\boldsymbol{O}_{\rm ttr}$ into the category with the highest probability. Then, the mean vectors of each Gaussian model that can most typically reflect the data distribution characteristics of each Gaussian model are selected to constitute the

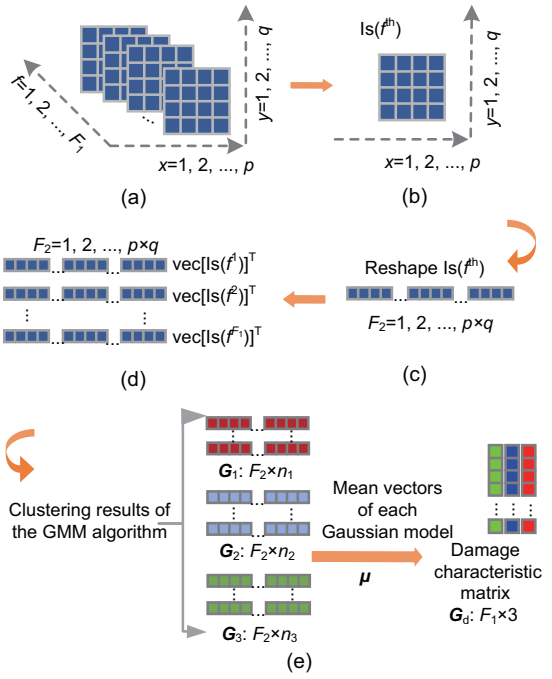

Fig. 2 Schematic of the data conversion and clustering: (a) image sequence Is(f); (b) $f^{\rm th}$ frame of Is(f); (c) vec[Is($f^{\rm th}$)]$^{\rm T}$; (d) reconstruction matrix $\boldsymbol{O}_{\rm ttr}$; (e) damage characteristic matrix construction

damage characteristic matrix $\boldsymbol{G}_{\rm d}$, which is shown in Fig. 2. The flowchart of the $\boldsymbol{O}_{\rm ttr}$ classification implemented by the GMM algorithm (Algorithm 1) is as follows:

As shown in Fig. 2e, the GMM algorithm is used to divide the reconstruction matrix $\boldsymbol{O}_{\rm ttr}$ into three clusters. The clustering results are $\boldsymbol{G}_1$, $\boldsymbol{G}_2$, and $\boldsymbol{G}_3$, which are combined into the damage characteristic matrix $\boldsymbol{G}_{\rm d}$ ($F_1 \times 3$).

3.2 Damage image reconstruction

When introducing the pseudo-inverse matrix $\boldsymbol{G}_{\rm d}^{\dagger}$, we obtain the observation result matrix $\boldsymbol{O}_{\rm r}$ ($n \times M$) of $\boldsymbol{G}_{\rm d}$ under the reconstruction matrix $\boldsymbol{O}_{\rm ttr}$ conditions by $\boldsymbol{O}_{\rm r} = \boldsymbol{O}_{\rm ttr}^{\rm T}(\boldsymbol{G}_{\rm d}^{\dagger})^{\rm T}$, which can highlight all kinds of characteristic information. Similarly, matrix $\boldsymbol{O}_{\rm r}$ is converted back to the original image size to reconstruct various images of typical characteristics. As shown in Fig. 3, matrix $\boldsymbol{O}_{\rm r}$ is reconstructed into three types of characteristic images ($\boldsymbol{O}_{\rm r_1}, \boldsymbol{O}_{\rm r_2}, \boldsymbol{O}_{\rm r_3}$). Each type represents a different detection area location.

The essence of the damage reconstructed image (DRI) is a matrix that contains temperature information. Based on the reconstructed temperature

Algorithm 1 GMM clustering algorithm for TTRs

Require: the reconstruction matrix $\boldsymbol{O}_{\mathrm{ttr}}$ and the number of clusters M

Ensure: the damage characteristic matrix $\boldsymbol{G}_{\mathrm{d}}$

1: Initial value setting: $\boldsymbol{O}_{\mathrm{ttr}}$ is classified and expressed as $\boldsymbol{O}_{\mathrm{ttr}}(:,i)$ $(i=1,2,...,n)$. Randomly set the initial value of mean vectors $\boldsymbol{\mu}_m$, where $m=1,2,\cdots,M$.

2: Establish the Gaussian mixture probability density function. Eq. (A1) can be used to approximate the complex distribution of TTRs:

$$p\left(\boldsymbol{o}_i|\theta^v\right)=\sum_{m=1}^{M}\alpha_{im}^{v}p_m\left(\boldsymbol{o}_i|\boldsymbol{\mu}_m^v,\boldsymbol{\Sigma}_m^v\right), \tag{A1}$$

where α_{im} is the mixing coefficient and $\sum_{m=1}^{M}\alpha_{im}=1$ $(i=1,2,...,n)$, $\boldsymbol{o}_i\in\{\boldsymbol{O}_{\mathrm{ttr}}(:,1),\boldsymbol{O}_{\mathrm{ttr}}(:,2),\cdots,\boldsymbol{O}_{\mathrm{ttr}}(:,n)\}$, and $\theta=\{\boldsymbol{\mu}_1,\boldsymbol{\mu}_2,...,\boldsymbol{\mu}_M,\boldsymbol{\Sigma}_1,\boldsymbol{\Sigma}_2,...,\boldsymbol{\Sigma}_M\}$ denotes the parametric vector set of mean vector $\boldsymbol{\mu}$ and covariance matrix $\boldsymbol{\Sigma}$.

3: Calculate the posterior probability of $\boldsymbol{o}_i$ coming from the m^{th} Gaussian mixture distribution. Use Eq. (A2) to find the posterior probability of $\boldsymbol{o}_i$ coming from the m^{th} Gaussian mixture distribution:

$$\beta_{im}^{v}=p\left(m|\boldsymbol{o}_i,\theta^v\right)=\frac{\alpha_{im}^{v}p_m\left(\boldsymbol{o}_i|\boldsymbol{\mu}_m^v,\boldsymbol{\Sigma}_m^v\right)}{\sum_{m=1}^{M}\alpha_{im}p_m\left(\boldsymbol{o}_i|\boldsymbol{\mu}_m,\boldsymbol{\Sigma}_m\right)}. \tag{A2}$$

4: The logarithmic likelihood function $L(\theta,\theta^v)$ is used to carry out iterative calculation of θ. It is calculated by Eq. (A3):

$$\begin{aligned}L(\theta,\theta^v)=&\sum_{m=1}^{M}\sum_{i=1}^{n}p(m|\boldsymbol{o}_i,\theta^v)\ln\alpha_{im}\\&+\sum_{m=1}^{M}\sum_{i=1}^{n}p(m|\boldsymbol{o}_i,\theta^v)\ln p_m(\boldsymbol{o}_i|\theta)\ .\end{aligned} \tag{A3}$$

Update parameter θ^{v+1} using the following formula:

$$\theta^{v+1}=\arg\max_{\theta}L\left(\theta,\theta^v\right). \tag{A4}$$

5: The cluster mark of each sample $\boldsymbol{o}_i$ is determined by $G_m=\arg\max_{m\in\{1,2,...M\}}\beta_{im}$, and is divided into the corresponding clusters.

6: The mean vectors of each G_m cluster are combined to form the damage characteristic matrix.

information represented by each element in the matrix, a mapping is formed to the color space. In DRIs, the damage characteristic area is reconstructed in red and the background area is blue.

4 Mosaicking module

We propose a mosaicking scheme for DRIs, despite a wide range of detecting requirements, which can realize complete integration of globally detected information on a large scale. First, considering its detection speed and robustness, the ORB algorithm is applied. Then, after the initial rough matching method with Euclidean distance calculation, numerous mismatches, which will seriously affect the precision and effect of mosaicking, need to be removed. To accomplish this task, an optimization algorithm, such as the MSAC algorithm, is used to search for inliers.

However, in the conventional MSAC algorithm, the threshold is set empirically by researchers, which is extremely uncertain and time-consuming. Therefore, we propose an adaptive threshold-setting method to obtain the optimized feature matching results to ensure the accuracy of mosaicking. In this section, a detailed algorithm description is provided and the schematic of DRI mosaicking is shown in Fig. 4.

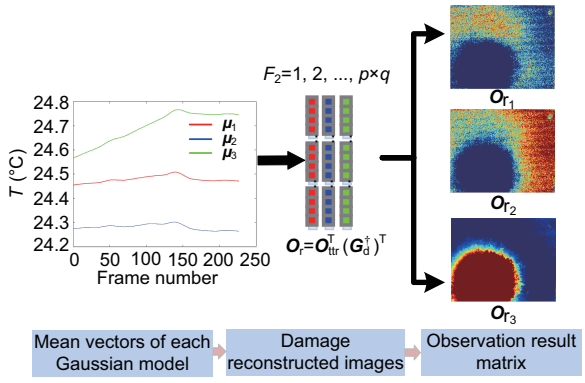

Fig. 3 Diagram sketch of image reconstruction (References to color refer to the online version of this figure)

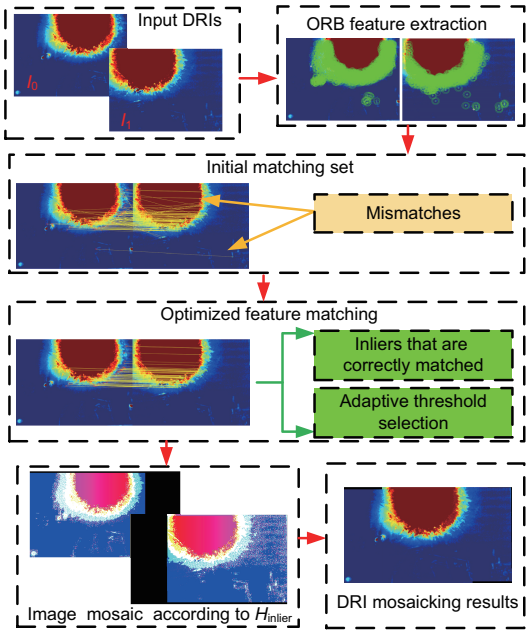

Fig. 4 Schematic of the image mosaicking scheme

4.1 ORB feature extraction algorithm for DRIs

The ORB method is improved on the basis of the FAST detector and BRIEF descriptor. Conventional FAST-16 with a circular radius of 16 is adopted here; it is favorable due to the performance boost that it can offer. For a local area of damage in a DRI, the absolute pixel value difference between point P and the pixel point in the dashed line in Fig. 5 is greater than a given threshold; that is, Eq. (1) is satisfied:

$$D=\begin{cases}1, & \text{if } |I(x)-I(p)|>\varepsilon,\\ 0, & \text{otherwise,}\end{cases} \tag{1}$$

where $I(x)$ represents the grayscale value of a pixel point on the circumference, $I(p)$ represents the grayscale value of target pixel p, and ε is a predetermined threshold.

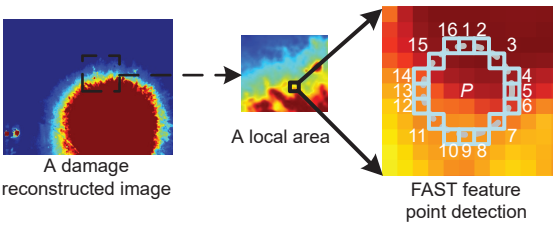

Fig. 5 Feature detection vs. feature point detection

An intensity centroid is employed to make FAST robust against orientations. An assumption is made that the intensity of the corner is offset from its center and that it subsequently uses this vector to add an orientation. The moments M_{pq} of a patch used to compute the centroid are represented as follows: $M_{pq}=\sum_{x,y}x^p y^q I(x,y)$. The centroid can be obtained as $\boldsymbol{C}=(C_x,C_y)=(\frac{M_{10}}{M_{00}},\frac{M_{01}}{M_{00}})$. Then, a vector can be constructed from O (center of the corner) to the centroid, and the orientation of the patch becomes $\theta=\arctan(\frac{C_x}{C_y})$. In the aforementioned equations, $I(x,y)$ is the grayscale value of point (x,y) and (C_x,C_y) is the centroid.

Consider the illustration of conventional BRIEF operations. Suppose that there is a smoothed image patch p. A binary test τ on this patch is represented as follows:

$$\tau(p;x,y)=\begin{cases}1, & p(x)<p(y),\\ 0, & p(x)\geq p(y),\end{cases} \tag{2}$$

where $p(x)$ denotes the intensity at a given point x. Hence, the feature can be written as a vector of n binary tests as follows:

$$f_n(P)=\sum\nolimits_{1\leq i\leq n}2^{i-1}\tau(p;x_i,y_i). \tag{3}$$

Consider any given feature set of n binary tests at a particular location, a $2\times n$ matrix can be represented as follows:

$$\boldsymbol{S}=\begin{pmatrix}x_1 & x_2 & \dots & x_n\\ y_1 & y_2 & \dots & y_n\end{pmatrix}. \tag{4}$$

Using the patch orientation θ and the corresponding rotation matrix $\boldsymbol{R}_\theta$, a steered version $\boldsymbol{S}_\theta$ of $\boldsymbol{S}$ can be written as $\boldsymbol{S}_\theta=\boldsymbol{R}_\theta\boldsymbol{S}$. Hence, the steered BRIEF operator can be represented as follows:

$$g_n(p,\theta):=f_n(P)|(x_i,y_i)\in\boldsymbol{S}_\theta. \tag{5}$$

The angle is discretized such that every angle is a multiple of $2\pi/30$ (12°). A lookup table of precomputed brief is constructed. The accurate set of points $\boldsymbol{S}_\theta$ will be used to compute the key point descriptor as long as key-point orientation θ is constant across all the directions.

4.2 Adaptive threshold selection method for MSAC

In this subsection, an adaptive threshold selection method is developed based on the MSAC algorithm. The MSAC algorithm model can be expressed as

$$e_i^2=\sum_i\left((\hat{x}_i-x_i)^2+(\hat{y}_i-y_i)^2\right), \tag{6}$$

$$p(e_i^2)=\begin{cases}e_i^2, & e_i^2<T^2,\\ \text{cost}, & e_i^2\geq T^2,\end{cases} \tag{7}$$

$$\text{cost}=\sum_i p(e_i^2), \tag{8}$$

where e_i^2 represents the difference between the i^{th} actual value of the data (x_i,y_i) and the theoretical value $(\hat{x}_i,\hat{y}_i)$, $p(e_i^2)$ is the data error weight, and "cost" is the overall error of the model sought, which is also called the cost function.

Detailed steps of the adaptive threshold selection method are as follows:

Step 1: For all the initial matching point pairs, calculate the cost function.

Step 2: Calculate and record the minimum, maximum, and mean values of the cost at step 1 as $E_{\min}$, $E_{\max}$, and E_{mean}, respectively.

Step 3: K, the number of thresholds T, is considered in the range from $E_{\min}$ to $E_{\max}$, where the value of K determines the range of the threshold. The step size of the adjacent threshold is calculated as $\partial = \frac{E_{\max}-E_{\min}}{K}$, and in accordance with $T(k) = (\partial \times k) + E_{\min}$ $(k = 1 : \partial : K)$, the value of each threshold is determined.

Step 4: For K threshold values, two classes are determined, and for each matching point pair, cost is calculated. According to the selected threshold value and the calculated cost, the matching point pairs are divided into two categories (the correct matching is the first category and the incorrect matching is the second category).

Step 5: To decrease the variance in the first category (correct matches) and to increase the variance in the second category, distance values must be close to each other in the first category. The mean value E_{mean} is also taken into account, where the threshold value should be close to the average value. The objective function is implemented as

$$f(k) = \frac{\delta_{1k}^2 + |E_{\text{mean}} - T(k)|}{\delta_{2k}^2}, \tag{9}$$

where δ_{1k}^2 is the k^{th} variance value in the first class and δ_{2k}^2 is the k^{th} variance in the second class.

Finally, the threshold with the lowest value $\min f(k)$ is selected as the final threshold according to Eq. (9). The optimal inlier point set N_{inlier} and candidate homography H_{inlier} are selected, and the infrared reconstruction image mosaicking process is further implemented based on the homography H_{inlier}.

5 Damage quantitative assessment module

In this section, a two-stage damage information segmentation method is proposed to achieve a complete extraction of the damage areas. The flowchart is shown in Fig. 6.

5.1 Segmentation and extraction of damage characteristic regions

The color feature difference of the damage reconstructed image directly reflects the different characteristic areas, so we can apply a clustering segmentation algorithm to segment the regions with damage characteristic color features (orange to red).

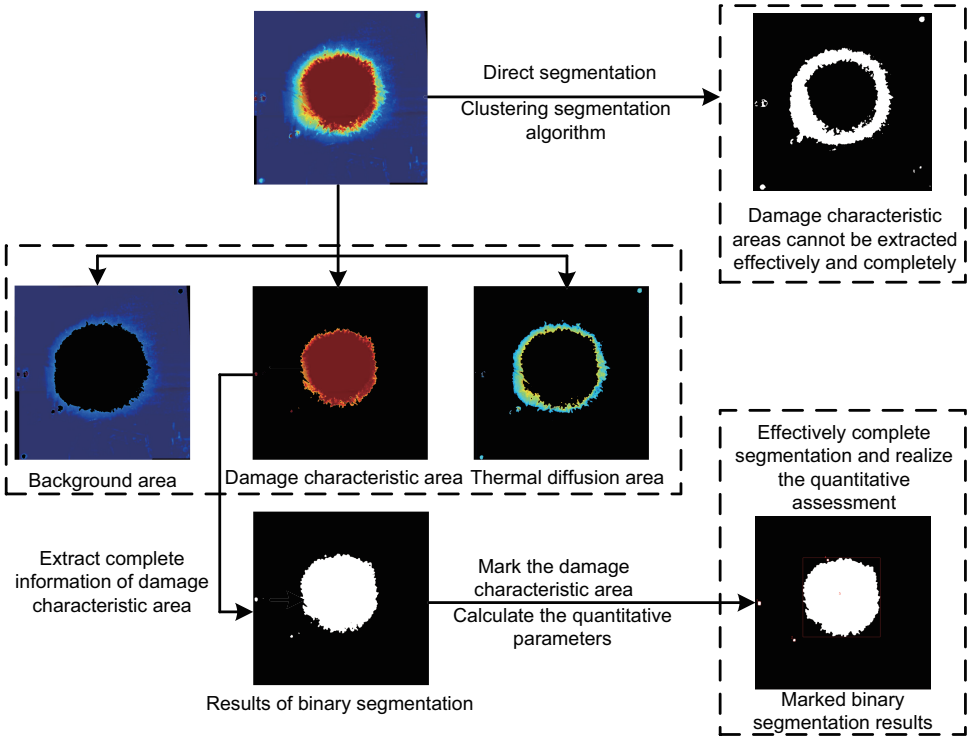

Fig. 6 Flowchart of the quantitative assessment method (References to color refer to the online version of this figure)

First, the input DRI is converted to the Lab color space, and it is recorded as a color feature object set $D(a_i,b_i)$ $(i=1,2,...,n)$, where n is the number of DRI pixels. The goal of K-means clustering is to divide $D(a_i,b_i)$ into K categories and form the damage feature data set $C_{\mathrm{d}}=\{c_k|k=1,2,...,K\}$, where the cluster center of c_k is o_k. Define the Euclidean distance measurement color difference criterion as

$$\psi(D(a_i,b_i),o_k)=\sqrt{\sum_{i=1}^{n_k}\left(D(a_i,b_i)-o_k\right)^2},\ D(a_i,b_i)\in c_k. \tag{10}$$

Based on Eq. (10), there are n_k color feature object sample points that are divided into category c_k. Take the average value of all sample points in the class subset c_k as the class center o_k. The iterative update calculation method is as follows:

$$o_k=\frac{1}{n_k}\sum_{D(a_i,b_i)\in c_k}D(a_i,b_i). \tag{11}$$

Calculation is repeated until the color difference takes the minimum value, which means that the sum of the distances from each sample data to its cluster center point takes the minimum value. If o_k in Eq. (11) goes to the minimum, the judgment algorithm is terminated and the damage characteristic data set C_{d} is taken as the final clustering segmentation result.

The cluster segmentation image reflects the different DRI area information, in which the red damage characteristic region is separately extracted, removing the interference caused by the background and the lateral heat diffusion.

Moreover, we propose a binary segmentation extraction algorithm that is based on dual-threshold segmentation processing to ensure the segmentation accuracy and obtain complete segmentation results of damage characteristic regions. Suppose that the gray level set of its pixels is $g\in(0,1)$, that the number of all pixels in gray level i is denoted as g_i, and that the total number of pixels is N_{g_i}. Then, the probability that gray level i appears in the image can be expressed as $G_i=\frac{g_i}{N_{g_i}}$, where $G_i\geq 0,\sum_{i=1}^{N}G_i=1$. After dual-threshold (T_1,T_2) binarization segmentation, the pixels in the image are divided into three categories, C_{0-T_1}, $C_{T_1-T_2}$, and C_{T_2-1}. The probability distribution of various occurrence types is

$$\begin{cases} h_0{=}h_0(T_1)=P(C_{0-T_1})=\sum\limits_{i=0}^{T_1}P_i, \\ h_1{=}h_1(T_1T_2)=P(C_{T_1-T_2})=\sum\limits_{i=T_1}^{T_2}P_i, \\ h_2{=}h_2(T_2)=P(C_{T_2-1})=\sum\limits_{i=T_2}^{1}P_i. \end{cases} \tag{12}$$

The average values of various gray levels are as follows:

$$\begin{cases} \nu_0(T_1)=\sum\limits_{i=0}^{T_1}iP_i, \\ \nu_1(T_1T_2)=\sum\limits_{i=T_1}^{T_2}iP_i, \\ \nu_2(T_2)=\sum\limits_{i=T_2}^{1}iP_i, \\ \nu_{\mathrm{s}}=\sum\limits_{i=0}^{1}iP_i. \end{cases} \tag{13}$$

The expression for the variance between classes is as follows:

$$\chi_{\mathrm{c}}^2(T_1,T_2)=h_0\nu_0^2+h_1\nu_1^2+h_2\nu_2^2-\nu_{\mathrm{s}}^2. \tag{14}$$

Finally, the best threshold combination (T_1^*,T_2^*) is obtained as

$$\chi_{\mathrm{c}}^2(T_1^*,T_2^*)=\max_{0\leq T_1\leq T_2\leq 1}\left\{\chi_{\mathrm{c}}^2(T_1,T_2)\right\}. \tag{15}$$

From the best threshold combination (T_1^*,T_2^*), the damage characteristic region is segmented and marked as bright white, which achieves segmentation and extraction of damage information.

5.2 Localization and quantification of damage characteristic regions

By counting the number of pixel points in the connected domain of each damage characteristic region as "1," we compare the "1" pixels statistically and record the minimum and maximum horizontal and vertical coordinates as the upper-left corner coordinates $\mathrm{ul}(x,y)$ and the lower-right corner coordinates $\mathrm{lr}(x,y)$, respectively. We set the upper-left corner of the shooting range and the damage segmentation image as the starting point (1, 1) of the spatial position coordinates and the pixel coordinates.

Assume that the detection area is $M\times N$ and that the DRI with resolution $m\times n$ is segmented by the clustering segmentation algorithm and binarization segmentation algorithm. The equivalent proportional relations are expressed as $x'=\frac{x}{m}\times M, y'=$

$\frac{y}{n} \times N$. Fig. 7 shows the damage location. The actual spatial location information of the damage characteristic regions of the test piece is estimated based on the scale conversion of the position information of image pixel points.

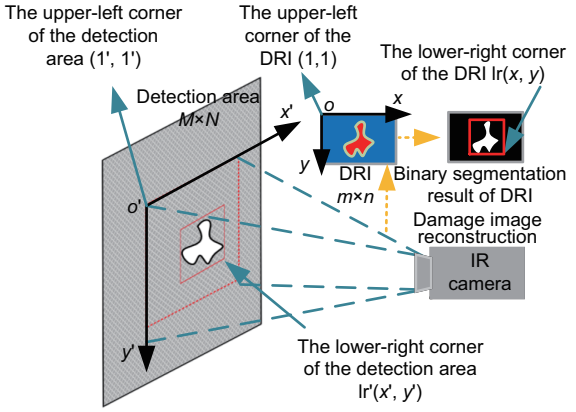

Fig. 7 Schematic of damage characteristic area localization

The perimeter conversion coefficient λ between the tested region and the DRI is the ratio of the actual perimeter $\mathrm{Pm_r}$ of the tested region to the perimeter value $\mathrm{Pm_p}$. The calculation formula is as follows:

$$\mathrm{Pm_{r\_d}} = \frac{\mathrm{Pm_r}}{\mathrm{Pm_p} \cdot \mathrm{Pm_{p\_d}}} = \lambda \cdot \mathrm{Pm_{p\_d}}, \qquad (16)$$

where $\mathrm{Pm_{p\_d}}$ and $\mathrm{Pm_{r\_d}}$ represent the calculated and actual perimeter values of a damage characteristic region, respectively.

6 Experimental results and discussion

6.1 Experiment of damage reconstruction

In the experiment, for sample A with HVI and sample B with artificial carbon fiber damage, we collected the infrared thermal data of local areas A1–A4 and B1–B4. We set the mixing coefficient of GMM as 3, divided the data, and recorded the mean vectors of the Gaussian distributions as $\boldsymbol{\mu}_1$, $\boldsymbol{\mu}_2$ and $\boldsymbol{\mu}_3$. The mean vector curves of different detection areas reflecting the same damage region were approximately the same and can be clearly distinguished. As shown in Tables 1 and 2, we further applied the reconstruction algorithm to obtain the DRIs of samples A and B, respectively.

6.2 Mosaicking results of reconstructed damage images

We carried out an experiment of the three methods (SIFT, SURF, and ORB) based on the Matlab2020a platform. By comparing the number of detection feature points and the time spent, the applicability and advantages of the algorithms can be determined.

Fig. 8 shows the experimental results of the feature extraction process of A1-A2 mosaicking. The three methods have extracted a considerable number of feature points. The experimental data statistics of the feature extraction algorithm is shown in Table 3. Among them, the feature points detected by the SIFT algorithm were distributed mainly at the edge feature contour of the impact damage and the number of feature points was considerable, but the detection time was too long. Meanwhile, compared with the ORB algorithm, the SURF algorithm had fewer feature points detected per unit time. In summary, for the mosaicking process of damage reconstructed images, the detection speed and efficiency of the ORB algorithm were better than their counterparts of the traditional SIFT and SURF methods.

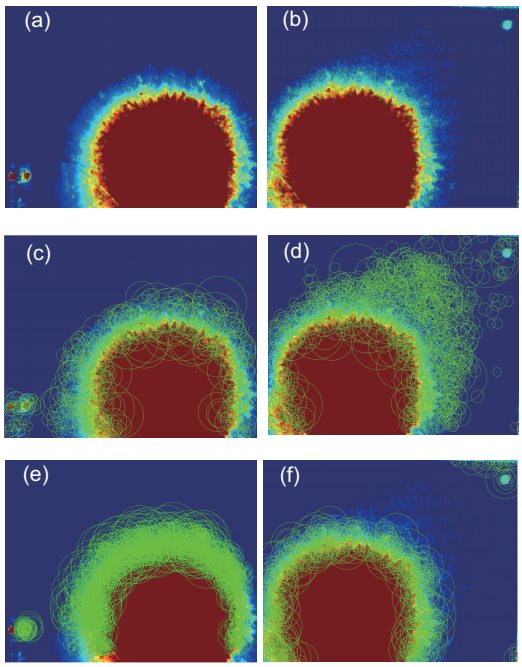

Fig. 8 Experimental result comparison of feature extraction algorithms: (a) SIFT for A1; (b) SIFT for A2; (c) SURF for A1; (d) SURF for A2; (e) ORB for A1; (f) ORB for A2

Table 1 Damage characteristic mean vector curves and the corresponding DRIs of sample *A*

Detection area	Damage characteristic curves	Damage reconstructed image
A1	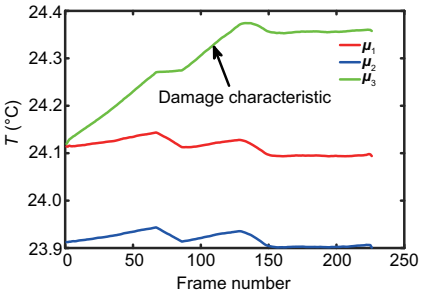	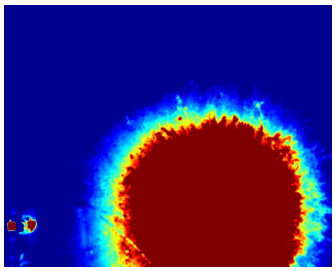
A2	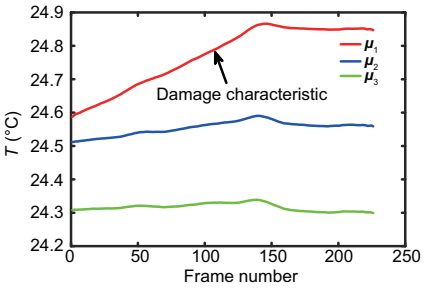	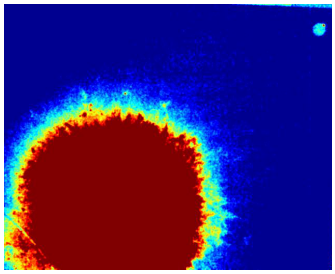
A3	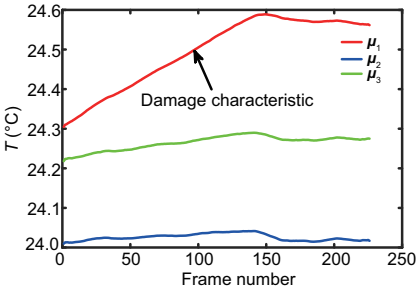	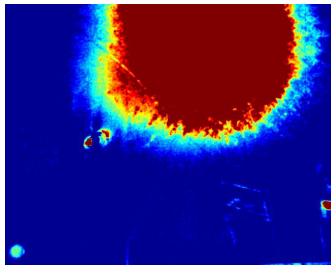
A4	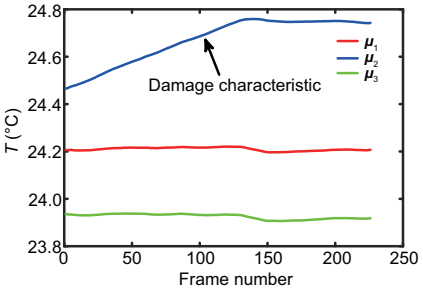	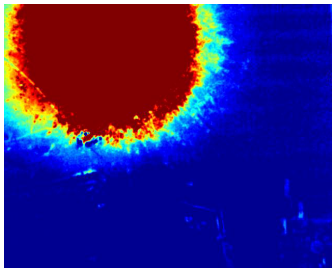

Table 2 Damage reconstructed images of sample *B*

B1	B2	B3	B4
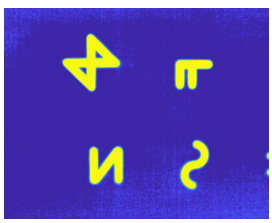	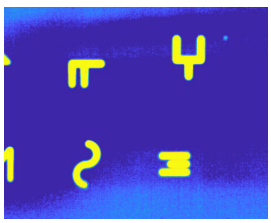	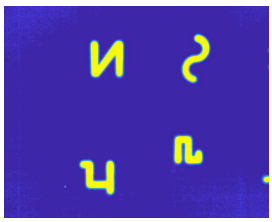	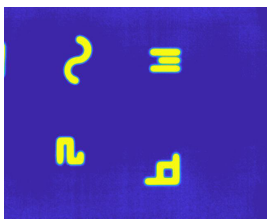

The root mean square error (RMSE) was selected to quantify the accuracy of homography H_{inlier} estimation, and it is defined as follows:

$$\text{RMSE}=\sqrt{\sum_{i=1}^{n}\frac{1}{n}\left\|N'_{\text{inlier}}-H_{\text{inlier}}N_{\text{inlier}}\right\|_2^2}. \tag{17}$$

The initial matching set obtained with the number 142 from the mosaicking process of A1-A2 was used as the input, and we found that the value of the adaptive threshold was 13.43. Next, as shown in Table 4, we set the threshold values to 1, 5, 10, 50, 100, and 13.43. It can be seen from Table 4 that when the threshold was set to 1, the inlier ratio was very small. When the threshold was set from 5 to 50, the ratios and RMSE values were almost the same and when the threshold value was set to 100, mismatches occurred and the RMSE value became large, which means that the mosaicking precision was low.

Finally, the specific mosaicking process of sample A is shown in Table 5. Similarly, the mosaicking results of sample B are shown in Fig. 9. From the final global mosaicking results of samples A and B, it can be seen that the mosaicking results were explicit, without deformation or distortion, reflecting the global damage characteristic distribution of the test samples. The experimental results proved the efficiency and applicability of the proposed method.

Table 3 Experimental results of the feature extraction algorithms

Process	Number			Time (s)		
	SIFT	SURF	ORB	SIFT	SURF	ORB
A1-A2	928/1717	713/1207	1279/2059	2.9318	0.8344	0.6503
A3-A4	1261/1131	998/1364	1817/1537	2.2267	0.6213	0.5461

Number means the number of detected feature points. At the feature point detection step, two images need to be processed. The left side of "/" represents the number of feature points detected in the reference image, and the right side represents the number of images to be mosaicked

Table 4 Comparison of mosaicking results for different thresholds

Threshold	Number of inliers	Inlier ratio	RMSE
1	50	0.33	0.4188
5	140	0.92	1.3557
10	142	0.93	1.3848
13.43	142	0.93	1.3848
50	142	0.93	1.3848
100	143	0.94	4.6928

RMSE: root mean square error

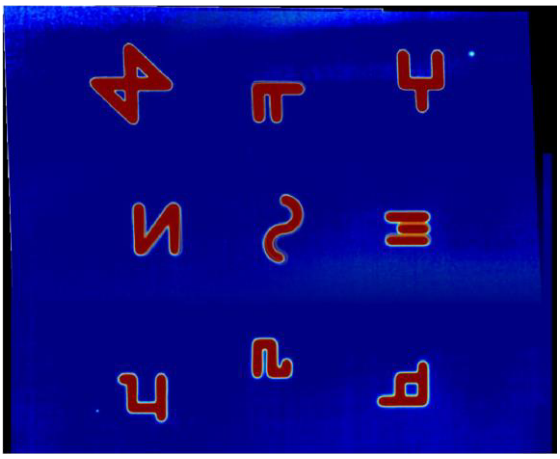

Fig. 9 Global mosaicking results of sample B

Table 5 Specific display of image mosaicking of sample A

Process	Initial feature matching	Optimized matching	Image mosaicking results
A1-A2	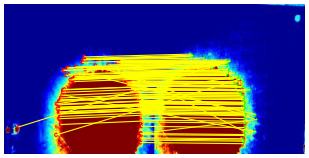	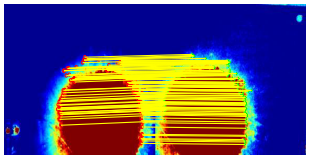	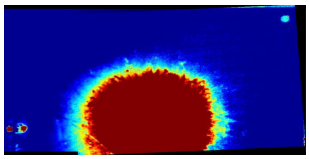
A3-A4	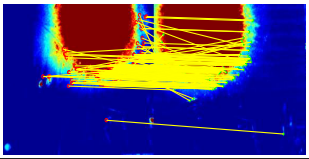	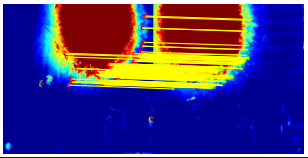	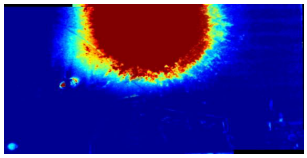
A1A2-A3A4	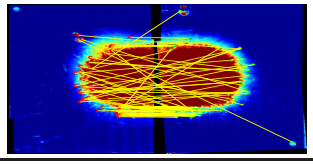	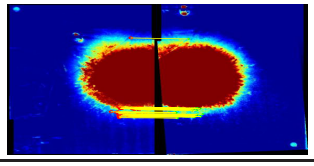	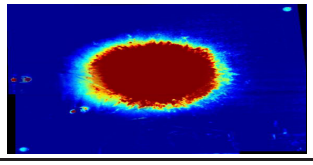

6.3 Damage quantitative assessment results

Fig. 10 shows the damage characteristic region segmentation extraction results of the global mosaicking based on the clustering segmentation algorithm in the Lab color space. Through the segmentation algorithm, the background noise of the test sample was removed and the lateral thermal diffusion interference caused by thermal radiation was reduced. The damage characteristic images were segmented to carry out further parameter calculation to achieve damage quantitative assessment.

Then, for the results obtained by the clustering segmentation algorithm, the binarized segmentation results of the damage characteristic area were further extracted. Because compared with single threshold processing, multi-threshold processing increases only the computational complexity and will involve more parameter adjustments, to facilitate verification and comparison of advanced methods, we introduced only the single-threshold principle. We listed the following state-of-the-art threshold-based segmentation algorithms as a comparison, namely, Otsu, the minimum error threshold method, one-dimensional maximum entropy threshold segmentation method, and two-dimensional maximum entropy threshold segmentation method.

The segmentation results of the four methods are shown in Fig. 11, and it can be seen that all the four methods can achieve segmentation and extraction of partial damage characteristic regions. The threshold results are shown after calculation and optimization of each threshold segmentation algorithm and the time spent on image segmentation is also provided. Compared with other threshold segmentation algorithms, the Otsu method had a great advantage in time consumption and the calculated threshold parameters can achieve partial effective segmentation of the damage characteristic areas. Therefore, based on the Otsu threshold segmentation algorithm, we used dual-threshold processing to achieve complete segmentation and extraction of the damage characteristic regions.

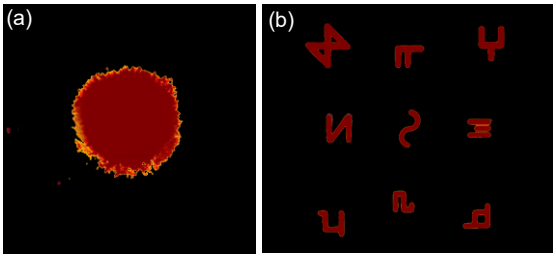

Fig. 10 Segmentation results of the clustering segmentation algorithm: (a) damage characteristic regions of sample *A*; (b) damage characteristic regions of sample *B*

As shown in Fig. 12, segmentation results of each damage characteristic region were surrounded by the smallest circumscribed rectangle delimited by the upper-left corner coordinates $\mathrm{ul}(x, y)$ and the lower-right corner coordinates $\mathrm{lr}(x, y)$. Both samples A and B were square plates of 1 m × 1 m, and the perimeter was denoted as 4 m. The reconstructed image mosaicking results of samples A and B showed that the characteristic parameters of perimeter were calculated as 3296.077 and 3200.316 respectively, and the resolutions were 855 × 845 and 883 × 752 respectively. Based on this, the conversion coefficients of perimeter were calculated as $\lambda_A = 1.21$ and $\lambda_B = 1.25$. Finally, the image damage

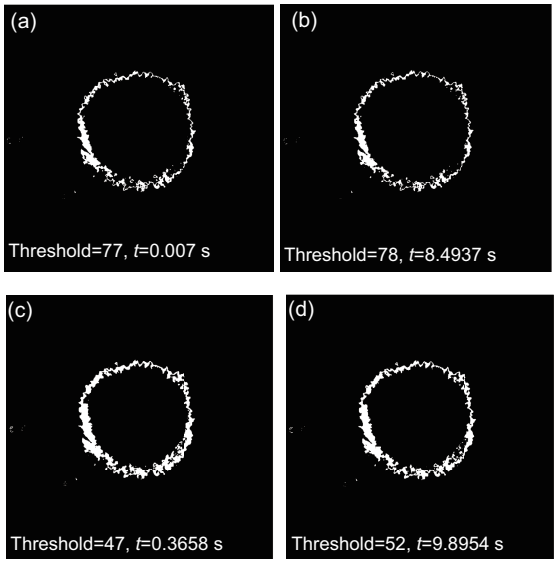

Fig. 11 Experimental result comparison of threshold segmentation algorithms: (a) Otsu; (b) minimum error threshold; (c) one-dimensional maximum entropy; (d) two-dimensional maximum entropy

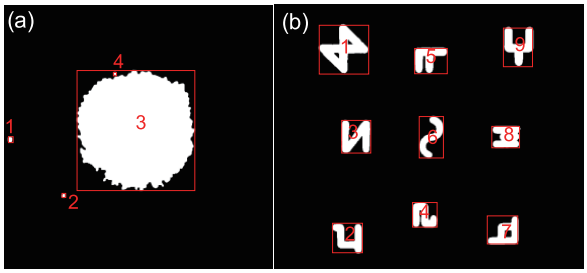

Fig. 12 Segmentation marking results of damage characteristic regions of samples *A* (a) and *B* (b)

characteristic regional coordinates and perimeter parameter $\mathrm{Pm_{p\_d}}$ were converted into the actual regional spatial position coordinates $\mathrm{lr}(x', y')$ and $\mathrm{ul}(x', y')$ and the actual damage perimeter $\mathrm{Pm_{r\_d}}$, respectively. A1–A4 and B1–B9 damage characteristic regions were extracted from samples A and B and the statistics is shown in Tables 6 and 7.

The actual regional spatial position coordinates correspond to the position information of each damage characteristic region in the test sample and reflect the damage distribution information. The actual damage perimeter value $\mathrm{Pm_{r\_d}}$ of each damage characteristic region obtained by conversion directly reflects the damage degree, thus realizing quantitative assessment of the damage information.

7 Conclusions

In this study, we proposed a quantitative damage assessment method for spacecraft based on the damage reconstructed image mosaic technology. Based on the GMM clustering algorithm, the damage characteristics were extracted from the infrared thermal video information to reconstruct the image. On this basis, an improved mosaicking scheme was proposed. Based on the global mosaicking results, the damage characteristic region was further segmented and extracted. Damage localization and quantitative calculation of the damage information were realized. The experimental results verified the efficiency and applicability of the quantitative assessment scheme.

Contributors

Kuo ZHANG and Jianliang HUO designed the research. Kuo ZHANG, Shengzhe WANG, and Xiao ZHANG processed the data. Kuo ZHANG and Jianliang HUO drafted the paper. Shengzhe WANG helped organize the paper. Xiao ZHANG and Yiting FENG revised and finalized the paper.

Compliance with ethics guidelines

Kuo ZHANG, Jianliang HUO, Shengzhe WANG, Xiao ZHANG, and Yiting FENG declare that they have no conflict of interest.

References

Adushkin V, Aksenov OY, Veniaminov S, et al., 2020. The small orbital debris population and its impact on space activities and ecological safety. *Acta Astronaut*, 176:591-597. https://doi.org/10.1016/j.actaastro.2020.01.015

Arnold J, Christiansen EL, Davis A, et al., 2009. Handbook for Designing MMOD Protection. Technical Report No. JSC-64399, Version A, National Aeronautics and Space Administration, Texas, USA.

Bay H, Ess A, Tuytelaars T, et al., 2008. Speeded-up robust features (SURF). *Comput Vis Image Underst*, 110(3):346-359. https://doi.org/10.1016/j.cviu.2007.09.014

Chandrakanth T, Sandhya B, 2015. Quality assessment of images using SSIM metric and CIEDE2000 distance methods in Lab color space. Proc 3rd Int Conf on Frontiers of Intelligent Computing: Theory and Applications, p.457-464. https://doi.org/10.1007/978-3-319-12012-6_50

Chen XR, Wang MN, Song ZJ, 2015. Global optimization surface-based registration for image-to-patient registration using Gaussian mixture model. *J Med Imag Health*

Table 6 Quantitative parameter statistics for damage characteristic regions of sample *A*

Area	$\mathrm{ul}(x, y)$	$\mathrm{ul}(x', y')$	$\mathrm{lr}(x, y)$	$\mathrm{lr}(x', y')$	$\mathrm{Pm_{p\_d}}$ (mm)	$\mathrm{Pm_{r\_d}}$ (mm)
A1	(13.5, 419.5)	(15.8, 495.0)	(28.5, 438.5)	(33.4, 517.4)	54.07	44.34
A2	(184.5, 600.5)	(215.9, 708.6)	(196.5, 613.5)	(229.9, 723.9)	38.27	31.38
A3	(232.5, 208.5)	(272.0, 246.0)	(608.5, 591.5)	(712.0, 698.0)	1573.30	1290.11
A4	(348.5, 214.5)	(407.8, 253.1)	(358.5, 225.5)	(419.5, 266.1)	31.81	26.08

Table 7 Quantitative parameter statistics for damage characteristics regions of sample *B*

Area	$\mathrm{ul}(x, y)$	$\mathrm{ul}(x', y')$	$\mathrm{lr}(x, y)$	$\mathrm{lr}(x', y')$	$\mathrm{Pm_{p\_d}}$ (mm)	$\mathrm{Pm_{r\_d}}$ (mm)
B1	(130.5, 58.5)	(147.5, 77.8)	(271.5, 197.5)	(306.8, 262.7)	454.32	567.90
B2	(168.5, 622.5)	(190.4, 827.9)	(253.5, 761.5)	(286.5, 1012.8)	382.13	477.66
B3	(194.5, 329.5)	(219.8, 438.2)	(277.5, 468.5)	(313.6, 623.1)	472.98	591.22
B4	(396.5, 563.5)	(448.0, 749.5)	(466.5, 702.5)	(527.1, 934.3)	350.55	438.18
B5	(402.5, 124.5)	(454.8, 165.6)	(495.5, 263.5)	(559.9, 350.5)	375.60	469.49
B6	(415.5, 318.5)	(469.5, 423.6)	(484.5, 457.5)	(547.5, 608.5)	347.48	434.35
B7	(609.5, 601.5)	(688.7, 800.0)	(696.5, 740.5)	(787.0, 984.9)	294.87	368.59
B8	(622.5, 346.5)	(703.4, 460.8)	(701.5, 485.5)	(792.7, 645.7)	302.75	378.44
B9	(655.5, 66.5)	(740.7, 88.4)	(738.5, 205.5)	(834.5, 273.3)	424.98	531.23

Inform, 5(8):1870-1874. https://doi.org/10.1166/jmihi.2015.1661

Cheng YH, Tian LL, Yin C, et al., 2018. Research on crack detection applications of improved PCNN algorithm in moi nondestructive test method. *Neurocomputing*, 277:249-259. https://doi.org/10.1016/j.neucom.2017.02.099

Dua G, Arora V, Mulaveesala R, 2021. Defect detection capabilities of pulse compression based infrared nondestructive testing and evaluation. *IEEE Sens J*, 21(6):7940-7947. https://doi.org/10.1109/JSEN.2020.3046320

Fida E, Baber J, Bakhtyar M, et al., 2017. Unsupervised image segmentation using Lab color space. Proc Intelligent Systems Conf, p.774-778. https://doi.org/10.1109/IntelliSys.2017.8324217

Gao B, Bai LB, Woo WL, et al., 2014. Automatic defect identification of eddy current pulsed thermography using single channel blind source separation. *IEEE Trans Instrum Meas*, 63(4):913-922. https://doi.org/10.1109/TIM.2013.2285789

Huang XG, Yin C, Dadras S, et al., 2018. Adaptive rapid defect identification in ECPT based on K-means and automatic segmentation algorithm. *J Amb Intell Human Comput*. https://doi.org/10.1007/s12652-017-0671-5

Huang XG, Yin C, Ru HQ, et al., 2020. Hypervelocity impact damage behavior of B_4C/Al composite for MMOD shielding application. *Mater Des*, 186:108323. https://doi.org/10.1016/j.matdes.2019.108323

Karnati S, Liou FF, 2020. Detection and tracking of melt pool in blown powder deposition through image processing of infrared camera data. In: Sergiyenko O, Flores-Fuentes W, Mercorelli P (Eds.), Machine Vision and Navigation. Springer, Cham, p.711-732. https://doi.org/10.1007/978-3-030-22587-2_22

Kaur K, Mulaveesala R, 2020. Efficient selection of independent components for inspection of mild steel sample using infrared thermography. *Electron Lett*, 56(19):990-993. https://doi.org/10.1049/el.2020.0618

Khan AA, Vrabie V, Mars JI, et al., 2008. A source separation technique for processing of thermometric data from fiber-optic DTS measurements for water leakage identification in dikes. *IEEE Sens J*, 8(7):1118-1129. https://doi.org/10.1109/JSEN.2008.926109

Lamb H, 2018. Space agencies turn focus on small space debris. *Eng Technol*, 13(1):48-49. https://doi.org/10.1049/et.2018.0104

Laraqui A, Saaidi A, Satori K, 2018. MSIP: multi-scale image pre-processing method applied in image mosaic. *Multimed Tools Appl*, 77(6):7517-7537. https://doi.org/10.1007/s11042-017-4659-0

Li Y, Ming AB, Mao H, et al., 2019. Detection and characterization of mechanical impact damage within multi-layer carbon fiber reinforced polymer (CFRP) laminate using passive thermography. *IEEE Access*, 7:27689-27698. https://doi.org/10.1109/ACCESS.2019.2902195

Liang T, Ren WW, Tian GY, et al., 2016. Low energy impact damage detection in CFRP using eddy current pulsed thermography. *Compos Struct*, 143:352-361. https://doi.org/10.1016/j.compstruct.2016.02.039

Lowe DG, 2004. Distinctive image features from scale-invariant keypoints. *Int J Comput Vis*, 60(2):91-110. https://doi.org/10.1023/B:VISI.0000029664.99615.94

Magri L, Fusiello A, 2017. Multiple structure recovery via robust preference analysis. *Image Vis Comput*, 67:1-15. https://doi.org/10.1016/j.imavis.2017.09.005

Qiu L, Fang F, Yuan SF, 2019. Improved density peak clustering-based adaptive Gaussian mixture model for damage monitoring in aircraft structures under time-varying conditions. *Mech Syst Signal Process*, 126:281-304. https://doi.org/10.1016/j.ymssp.2019.01.034

Rajic N, 2002. Principal component thermography for flaw contrast enhancement and flaw depth characterisation in composite structures. *Compos Struct*, 58(4):521-528. https://doi.org/10.1016/S0263-8223(02)00161-7

Richter F, Ries CX, Romberg S, et al., 2014. Partial contour matching for document pieces with content-based prior. Proc IEEE Int Conf on Multimedia and Expo, p.1-6. https://doi.org/10.1109/ICME.2014.6890237

Rublee E, Rabaud V, Konolige K, et al., 2011. ORB: an efficient alternative to SIFT or SURF. Proc Int Conf on Computer Vision, p.2564-2571. https://doi.org/10.1109/ICCV.2011.6126544

Smurov IY, Dubenskaya MA, Zhirnov IV, et al., 2016. Determination of the true temperature during selective laser melting of metal powders based on measurements with an infrared camera. *Meas Technol*, 59(9):971-974. https://doi.org/10.1007/s11018-016-1077-z

Surya Kumari D, Bhavani SA, 2017. A new iterative hybrid edge technique using image mosaic. In: Satapathy SC, Bhateja V, RajuK S, et al. (Eds.), Computer Communication, Networking and Internet Security. Springer, Singapore, p.235-243. https://doi.org/10.1007/978-981-10-3226-4_23

Yin C, Xue T, Huang XG, et al., 2019. Research on damages evaluation method with multi-objective feature extraction optimization scheme for M/OD impact risk assessment. *IEEE Access*, 7:98530-98545. https://doi.org/10.1109/ACCESS.2019.2930114

Yin C, Huang XG, Cao JW, et al., 2021. Infrared feature extraction and prediction method based on dynamic multi-objective optimization for space debris impact damages inspection. *J Franklin Inst*, 358(18):10165-10192. https://doi.org/10.1016/j.jfranklin.2021.10.039

Zhang HN, Huang XG, Yin C, et al., 2020. Design of hypervelocity-impact damage evaluation technique based on Bayesian classifier of transient temperature attributes. *IEEE Access*, 8:18703-18715. https://doi.org/10.1109/ACCESS.2020.2968398

Zhang WP, Li XJ, Yu JF, et al., 2018. Remote sensing image mosaic technology based on SURF algorithm in agriculture. *EURASIP J Image Video Process*, 2018:85. https://doi.org/10.1186/s13640-018-0323-5